communications physics

ARTICLE

https://doi.org/10.1038/s42005-023-01155-7 OPEN

Exchange field enhanced upper critical field of the superconductivity in compressed antiferromagnetic $EuTe_2$

Hualei Sun[1], Liang Qiu[1], Yifeng Han[2], Yunwei Zhang[1], Weiliang Wang[3], Chaoxin Huang[1], Naitian Liu[1], Mengwu Huo[1], Lisi Li[1], Hui Liu[1], Zengjia Liu[1], Peng Cheng[4], Hongxia Zhang[4], Hongliang Wang[5], Lijie Hao[5], Man-Rong Li[2], Dao-Xin Yao[1], Yusheng Hou[1], Pengcheng Dai[6] & Meng Wang[1✉]

Understanding the interplay between superconductivity and magnetism has been a long-standing challenge in condensed matter physics. Here we report high pressure studies on the *C*-type antiferromagnetic semiconductor $EuTe_2$ up to 36.0 GPa. A structural transition from the *I4/mcm* to the *C2/m* space group is identified at ~16 GPa. Superconductivity is observed above ~5 GPa in both structures. In the low-pressure phase, magnetoresistance measurements reveal strong couplings between the local moments of Eu^{2+} and the conduction electrons of Te 5*p* orbits. The upper critical field of superconductivity is well above the Pauli limit. While $EuTe_2$ becomes nonmagnetic in the high-pressure phase and the upper critical field drops below the Pauli limit. Our results demonstrate that the high upper critical field of $EuTe_2$ in the low-pressure phase is due to the exchange field compensation effect of Eu^{2+} and the superconductivity in both structures may arise in the framework of the Bardeen-Cooper-Schrieffer theory.

[1] Center for Neutron Science and Technology, Guangdong Provincial Key Laboratory of Magnetoelectric Physics and Devices, School of Physics, Sun Yat-Sen University, Guangzhou, Guangdong 510275, China. [2] Key Laboratory of Bioinorganic and Synthetic Chemistry of Ministry of Education, School of Chemistry, Sun Yat-Sen University, Guangzhou, Guangdong 510275, China. [3] School of Physics, Guangdong Province Key Laboratory of Display Material and Technology, Sun Yat-Sen University, Guangzhou, Guangdong 510275, China. [4] Laboratory for Neutron Scattering and Beijing Key Laboratory of Optoelectronic Functional Materials and MicroNano Devices, Department of Physics, Renmin University of China, 100872 Beijing, China. [5] China Institute of Atomic Energy, PO Box-275-30, 102413 Beijing, China. [6] Department of Physics and Astronomy, Rice Center for Quantum Materials, Rice University, Houston, TX, USA. ✉email: wangmeng5@mail.sysu.edu.cn

Superconductivity in conventional Bardeen-Cooper-Schrieffer (BCS) superconductors arises from electron-lattice interaction without the involvement of magnetism[1]. Below the superconducting (SC) transition temperature, electrons form coherent spin singlet cooper pairs that can be suppressed by a Pauli-limited magnetic field. In contrast, one of the hallmarks of unconventional superconductivity is the interplay between magnetism and superconductivity. For example, superconductivity in copper oxide and iron-based high-temperature superconductors occurs near long-range magnetic order where the 3*d* electrons of the transition metals across the Fermi level contribute to both the magnetic correlations and superconductivity[2–6]. In some unconventional superconductors, electron pairing forms spin-singlet and the upper critical field needed to suppress superconductivity is also Pauli limited[2–6]. For unconventional superconductivity with an upper critical field exceeding the Pauli limit, such as recently discovered UTe_2[7,8], electron pairing is believed to be spin triplets instead of singlets. In both spin-singlet and spin-triplet superconductors, magnetic fluctuations play an important role in the formation of cooper pairs as evidenced by the neutron spin resonance from inelastic neutron scattering spectra[6,9].

Although the mechanism of superconductivity for conventional and unconventional superconductors may be fundamentally different, both superconductors can host magnetic local moments not directly associated with SC layers. For example, in a class of iron-based superconductors consisting of Eu^{2+}, the 4*f* electrons with spin $S = 7/2$ could form an antiferromagnetic (AFM) or ferromagnetic sublattice coexisting and interacting with the magnetic sublattice of Fe[10,11]. However, the localized magnetism of Eu^{2+} does not interplay with the superconductivity seriously. For BCS superconductors such as RNi_2B_2C series (R = Y, Er, Ho, etc)[9], the interplay between the magnetic order of the rare earth layers and superconductivity can dramatically affect the physical properties of the system including the upper critical field needed to suppress superconductivity.

Previously, our group reported an antiferromagnetically colossal magnetoresistance $EuTe_2$ with a Néel temperature of $T_N = 11.4$ K and a thermal-activation gap of 16.24 meV at atmospheric pressure[12]. The magnetic field drives polarization of the local moments of Eu^{2+} and results in the reconstruction of the Te 5*p* orbitals[12,13]. It is interesting to explore the pressure effect on the small gap colossal magnetoresistance compound and investigate the interplay of the Eu^{2+} local moments with itinerant electrons of Te. Based on previous studies on $CrSiTe_3$, WTe_2, $EuIn_2As_2$, and $EuSn_2As_2$, superconductivity may emerge and the valent state transition from Eu^{2+} to Eu^{3+} may occur for $EuTe_2$ under pressure[14–17]. Very recently, a high-pressure study on $EuTe_2$ up to 12.0 GPa indeed reveals superconductivity and suggests the SC pairing mechanism is exotic[18].

Here, we present comprehensive experimental and theoretical investigations on $EuTe_2$ under pressure up to 36.0 GPa. Neutron diffraction measurements demonstrate $EuTe_2$ exhibits a *C*-type AFM order below T_N. A pressure-induced structural transition at ~16 GPa is discovered. In the low-pressure (LP) phase, the *C*-type AFM transition temperature T_N increases due to the enhancement of the magnetic exchange interactions of the compressed lattice. The thermal activation gap E_a is closed progressively, and superconductivity emerges above 5.0 GPa. The SC transition temperature T_cs spanning between 3~6 K in the pressure range of 5~27 GPa is irrespective of the structural transition and magnetism. While the upper critical field $\mu_0 H_{c2}$ for the superconductivity of the AFM LP phase is significantly larger than that of the superconductivity of the nonmagnetic high pressure (HP) phase. The $\mu_0 H_{c2}$ is affected by the microscopic spin texture of the Eu sublattice. The highest $\mu_0 H_{c2}$ is estimated to be 21.6 T for the spin-flipped state at 7.0 GPa. The ultra-high $\mu_0 H_{c2}$ could be understood by the compensation effect of the exchange field of Eu^{2+}, the so-called Jaccarino and Peter mechanism[19]. Our results, therefore, establish the pressure-temperature phase diagram of $EuTe_2$ and demonstrate the interesting interplay mechanism between Eu magnetic order, superconductivity, and pressure-induced structural lattice distortion.

Results

High-pressure structure. Figure 1 displays the in situ high-pressure synchrotron powder x-ray diffraction (XRD) patterns of $EuTe_2$ up to 36.0 GPa at room temperature and the refined crystal structures below 15.9 GPa and above 17.9 GPa, defined as the LP phase and HP phase, respectively. The LP phase can be indexed by the tetragonal *I4/mcm* space group (No. 140), identical to the ambient pressure crystal structure. The divalent europium is coordinated by eight nearest-neighbor tellurium ions[12]. The edge-sharing octagonal units form the layers of the tetragonal crystal structure as shown in Fig. 1c.

In terms of the diffraction peaks changed under pressure, an obvious structural phase transition between 15.9 and 17.9 GPa could be identified. We conducted an extensive search on the HP structure of $EuTe_2$ in the pressure range of 0 − 25 GPa via the

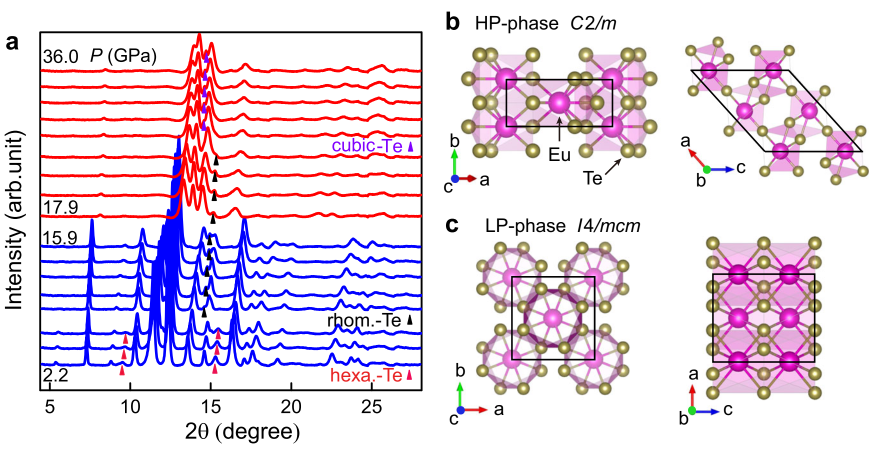

Fig. 1 X-ray diffraction (XRD) patterns and refined structures of $EuTe_2$ under pressure. a High-pressure XRD patterns of $EuTe_2$ from 2.2 to 36.0 GPa with an x-ray wavelength of 0.6199 Å. The XRD patterns of the LP phase are in blue and that of the HP phase are in red. Tellurium undergoes two structural phase transitions within the measured pressure. The peaks from the Te impurity are marked by the triangles. **b** Crystal structures of the high pressure (HP) phase and (**c**) the low pressure (LP) phase of $EuTe_2$.

CALYPSO method[20–22]. The monoclinic *C2/m* (No. 12) structure turns out to be a possible candidate for the HP phase at 17.9 GPa. Thus, we refined the experimental XRD pattern at 17.9 GPa by the Rietveld method through the *TOPAS*-Academic software[23]. The *C2/m* structure matches the XRD pattern of the HP phase well, as shown in Supplementary Fig. 1. Figure 1b shows the structure of the HP phase. The europium ions retain the eight-coordination but there is a significant deformation of the octagonal unit. This coordination unit exists in the compounds of Eu_3S_4 at atmospheric pressure, confirming that it is a stable coordination structure for europium chalcogenide[24]. Sulfur has a smaller ionic radius than tellurium, close to pressurized tellurium.

For the HP phase, slip occurs between the adjacent layers compared with the LP phase. As shown in Fig. 1b, c, the unit cell volume decreases sharply at the pressure-induced structural transition from 317.157(9) A^3 at 15.9 GPa to 262.524(3) A^3 at 17.9 GPa, which may be accompanied by the valent state transition from Eu^{2+} to nonmagnetic Eu^{3+}. The diffraction peaks and structural transitions of Te impurity can be observed in Fig. 1a[25,26]. The refined XRD patterns and structural parameters for 9.7 and 17.9 GPa are shown in Supplementary Note 1.

High-pressure electrical and magnetic properties. To investigate the electrical properties of $EuTe_2$ under pressure, we performed electrical transport measurements below 27.7 GPa. Figure 2a shows the temperature dependence of the resistance at various pressures, revealing semiconducting to metallic and SC transitions. Resistance as a function of pressure for selected temperatures is presented in Fig. 2b. The magnitude of the resistance decreases as pressure increases. The upturn in resistance at low pressure may be attributed to the scattering of conduction electrons by local moments of the Eu^{2+} ions. An abrupt drop in resistance appears between 14.7 and 16.2 GPa, consistent with the structural transition between 15.9 and 17.9 GPa. Thus, the structural transition pressure should occur at ~16.0 GPa. The resistance above ~50 K in Fig. 2a is fitted to the thermal activation-energy model $\rho(T) = \rho_0 \exp(E_a/k_B T)$, where ρ_0 is a prefactor, E_a is the thermal activation gap, and k_B is the Boltzmann constant. The gap of 16.24 meV for $EuTe_2$ at ambient pressure is gradually closed by pressure, as shown in Fig. 2c and Supplementary Note 2. The evolution of the carriers against pressure at 10 K is also investigated by the Hall resistance measurements. The Hall coefficient remains positive, revealing that the majority of carriers are holes (Supplementary Note 3). The determined density of holes shows an abrupt enhancement across the structural transition similar to the observation in $EuSn_2As_2$[17].

To elucidate the magnetic state of the HP phase, we conducted systematic magnetoresistance (MR) measurements against temperature and pressure. At ambient pressure, $EuTe_2$ shows colossal negative MR. Under pressure, the semiconducting gap is decreased, the resistance without a magnetic field becomes much smaller and the MR is suppressed accordingly (Supplementary Note 4). The integrated MRs (defined as $MR = (\rho_H - \rho_0)/\rho_0 \times 100\%$) over the magnetic fields from −10 to 10 T as presented in Fig. 2d decrease as pressure and temperature, diminishing gradually above 16.2 GPa. The abrupt decrease in MR suggests that the HP phase is not magnetically ordered.

Figure 3 shows the resistance in a smaller temperature range as a colormap on a logarithm scale. The T_N of the AFM transition and T_c of the SC transition under pressure could be identified from the resistance (Supplementary Note 5 and Note 6). Upon increasing pressure, the derived T_Ns increase from 11.4 K at ambient pressure to 16.7 K at 8.0 GPa. The superconductivity appears at 4.9 GPa with a T_c of 3.2 K, defined by the intersection of the tangent to the resistance curve during the transition process and the straight line of the normal state above the SC transition. The T_c reaches a maximum of 6.1 K at 7.0 GPa and decreases smoothly afterward across the structural transition,

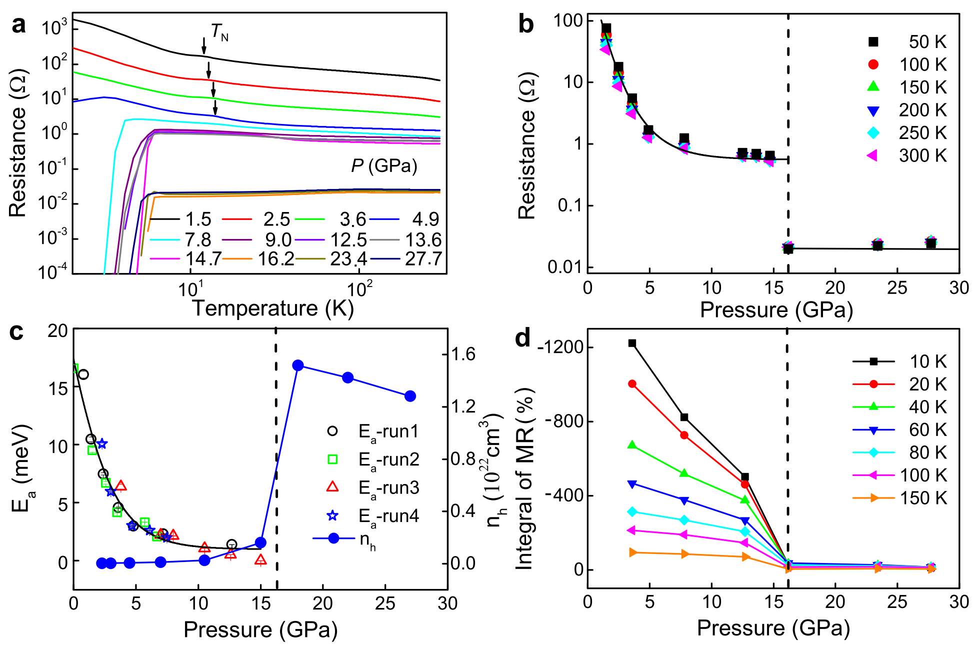

Fig. 2 Electrical transport properties under pressure. a Temperature dependence of the resistance upon pressures up to 27.7 GPa. The Néel transition temperatures (T_Ns) are labeled on low-pressure curves. **b** Pressure dependence of the resistance at various temperatures up to 300 K shown on a logarithm scale. **c** Thermal-activation gaps (E_as) derived from fittings of the resistance curves within the temperature range from 60 to 300 K using $\rho(T) = \rho_0 \exp(E_a/k_B T)$, where k_B is the Boltzmann constant. Different shapes of data points are measured on different samples. The black solid line is a guide to the eyes. The right axis represents the scale of carrier density. Error bars originating from the fitting process are smaller than the data points. **d** Integrals of magnetoresistance (MR) over the magnetic fields from −10 to 10 T as a function of pressure for selected temperatures. The dashed lines in (**b**–**d**) at 16.0 GPa mark the pressure of the structural transition.

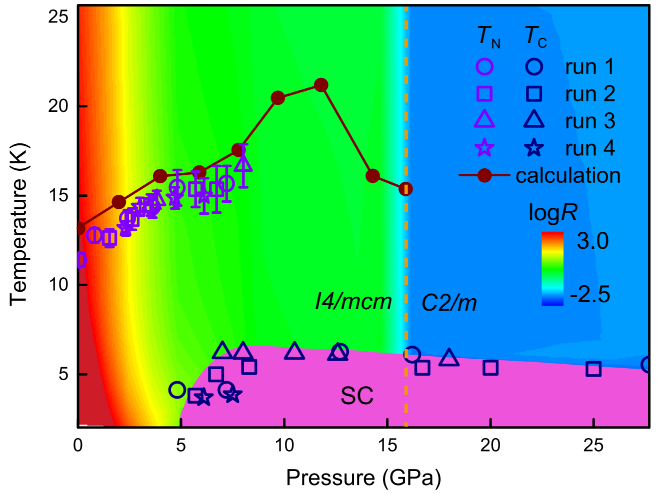

Fig. 3 A phase diagram of magnetism and superconductivity under pressure. The antiferromagnetic transition temperature T_N and superconducting (SC) transition temperature T_c against pressure. The filled circles are calculated T_Ns. The color represents different resistance on a logarithm scale. Different shapes of data points are obtained from different measurements. The errors of the T_Ns are estimated from resistance measurements.

indicating that the AFM order and spin fluctuations of Eu^{2+} have not contributed to the cooper pairing mechanism directly.

At ambient pressure and low temperature, the calculated energy difference between the *A*-type AFM and the *C*-type AFM is almost neglectable (about 1.5 meV per Eu)[12]. Neutron diffraction measurements were employed to distinguish the two magnetic structures. Although the neutron absorption from Eu atoms is serious, the magnetic reflections associated with the *C*-type AFM are observed unambiguously (Supplementary Note 7). To understand the underlying mechanism for the enhanced T_N in compressed $EuTe_2$, we investigate its exchange couplings based on the following spin model:

$$H = \sum_{\langle ij \rangle} J_{ij} \boldsymbol{S}_i \cdot \boldsymbol{S}_j + A \sum_i \left(S_i^z\right)^2. \tag{1}$$

Considering the small gap of $EuTe_2$, six nearest-neighbor (NN) Heisenberg exchange couplings are considered. In Eq. (1), A is the single-ion magnetic anisotropy parameter. For $EuTe_2$ at ambient pressure, our density functional theory (DFT) calculations show that it exhibits a *C*-type AFM ground state with a small gap of 18 meV and out-of-plane magnetic easy axis, consistent with our neutron scattering measurements. Our Monte Carlo simulations reveal the T_N is 13.17 K close to previous studies[12]. Under pressure, both the DFT calculations and Monte Carlo simulations indicate that the ground state is also the *C*-type AFM order. Four NN exchange couplings are strengthened obviously in regard to ferromagnetic ($J < 0$) or antiferromagnetic ($J > 0$) terms up to 11.8 GPa (Supplementary Table 2). This is understandable because the distances between the Eu^{2+} ions decrease under pressure. Correspondingly, the calculated T_Ns increase from 13.17 to 21.21 K at 11.8 GPa as shown in Fig. 3. For higher pressures near the structural transition, the Ruderman-Kittel-Kasuya-Yosida interaction may involve and lower the third and fourth NN exchange couplings, resulting in the decrease of the T_N.

Spin state transitions and high upper critical field. Superconductivity emerges in both the LP and HP phases, which have distinct structures and magnetic ground states. To explore the role of the local moments of Eu^{2+} in superconductivity, we conducted resistance measurements at 7.0 and 18.0 GPa. Figure 4a, b shows the resistance as a function of the magnetic field and temperature at 7.0 GPa. A color map of the resistance is plotted in Fig. 4c. The *C*-type AFM structure of $EuTe_2$ at ambient pressure undergoes a spin-flop transition at ~3.0 T and a spin-flip transition at ~8.0 T[12]. The magnetic fields for the spin-flop and spin-flip transitions below the T_N of 15.6 K at 7.0 GPa are extracted from the resistance in Fig. 4a, yielding 5.5 T for the spin-flop and 12.5 T for the spin-flip transitions at 5 K (Supplementary Note 8). The increased magnetic fields compared with that at ambient pressure are proportional to the increase of T_N. The SC transition temperatures T_cs at 7.0 GPa are determined from the resistance shown in Fig. 4b and displayed in Fig. 4c (Supplementary Note 9). We find the $\mu_0 H_{c2} - T_c$ relation does not follow a simple Ginzburg-Landau (GL) formula, $\mu_0 H_{c2}(T) = \mu_0 H_{c2}(0)[1 - (\frac{T}{T_c})^2]$. The experimentally determined T_cs against magnetic field could be separated into three segments, coincident with the AFM, spin flop, and spin flipped magnetic states. The $\mu_0 H_{c2}$s for the spin flop and spin flipped states are well above the Pauli limit of $\mu_0 H_{c2} = 1.84 \times T_c = 11.2$ T, where T_c is 6.1 K at 7.0 GPa and zero field[27]. We compare the resistance under various magnetic fields at 18.0 GPa in Fig. 4d. The colormap of resistance suggests that the HP phase is nonmagnetic. The $\mu_0 H_{c2}$ can be described by a single GL formula with the $T_c = 5.5$ K and $\mu_0 H_{c2} = 6.15$ T within the Pauli limit of 10.12 T.

Discussion

The superconductivity in $EuTe_2$ arising from Te impurity can be excluded because of the high upper critical field[28,29]. In some compounds consisting of Te, the $\mu_0 H_{c2}$ could achieve the magnitude of several teslas, such as $CrSiTe_3$, WTe_2, $HfTe_5$, Bi_2Te_3, and $CsBi_4Te_6$, where the normal states are not magnetically ordered[14,15,30–32]. The $\mu_0 H_{c2}$s of these compounds are still below the Pauli limit. UTe_2 superconducts below 1.6 K at ambient pressure with an ultra-high $\mu_0 H_{c2} > 45$ T[33]. The 5*f* electrons of uranium cross the Fermi level and contribute to the magnetism and superconductivity directly, resulting in the heavy Fermi property and possible triplet pairing mechanism[34,35].

Figure 5 shows the field dependence of T_cs in pressurized $EuTe_2$. The $\mu_0 H_{c2}$s are fitted for the experimentally determined AFM, spin flop, and spin flipped states to the GL formula, resulting in the upper critical fields of 10.1, 16.2, and 21.6 T, respectively. The Werthamer-Helfand-Hohenberg (WHH) formula of $\mu_0 H_{c2}(T) = -0.69 \times dH_{c2}/dT|_{T_c} \times T_c$ is also adopted to estimate the upper critical fields for the three distinct magnetic states, resulting in $\mu_0 H_{c2}$s of 10.7, 15.9, and 20.8 T, respectively[36,37]. The high $\mu_0 H_{c2}$s for the spin flop and spin flipped states may be attributed to the compensation effect of the exchange field H_J produced by the local moments of Eu^{2+}. We note for the spin-flipped state the direction of H_J is antiparallel to the direction of magnetic moments of Eu^{2+} on the Te sites. In this case, the net magnetic field H_T acting on the conduction electrons is $H_T = H_{c2} - |H_J|$[38]. As the Jaccarino-Peter mechanism, AFM spins do not contribute to the exchange field. The spin-flipped state with fully polarized moments of Eu^{2+} has the maximum H_J. If the sign of the coupling between the local spins and conduction electron spins is negative, the measured $\mu_0 H_{c2}$ should be larger than the Pauli limit[19]. As for $Eu_{0.75}Sn_{0.25}Mo_6S_{7.2}S_{0.8}$, an applied magnetic field can progressively tune the compound from SC to normal, to SC again, and finally back to the normal state below 1 K[39]. To estimate the Pauli limit critical field H_P and H_J of $Eu_{0.75}Sn_{0.25}Mo_6S_{7.2}S_{0.8}$ for the second SC phase with the lower and upper $\mu_0 H_{c2}$s at 4 and 22 T, we have the constraints of: (i) $4\,\mathrm{T} - \mu_0 H_J = -\mu_0 H_P$, and (ii)

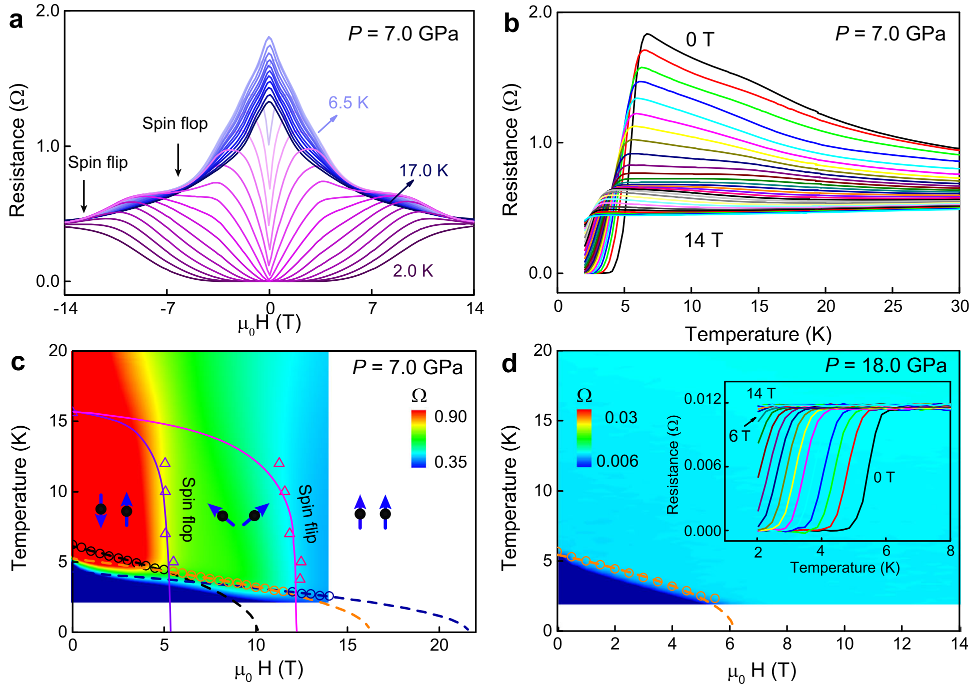

Fig. 4 Superconductivity and magnetism under pressure. a Magnetic field dependence of the resistance at 7.0 GPa and selected temperatures from 2.0 to 17.0 K. **b** Resistance from 2.0 to 30.0 K in different magnetic fields from 0 to 14.0 T measured every 0.5 T at 7.0 GPa. **c** A phase diagram with the antiferromagnetic order, spin flop, spin flip, and superconducting transitions. The solid lines are a guide for magnetic transitions. The dashed lines are the Ginzburg-Landau formula fittings to the segments of the superconducting transition temperatures. The color represents the magnitude of the resistance in (**b**) on a linear scale from 0.35 to 0.9 Ω. The magnetic fields of spin flop and spin-flip transitions are obtained from the magnetic field dependence of resistance in (**a**). **d** Phase diagram of the superconductivity against the magnetic field at 18.0 GPa. The inset is the resistance curves measured on selected magnetic fields. The color represents the magnitude of the resistance in the inset of (**d**) on a linear scale from 0.006 to 0.03 Ω. The dashed line is fitting to the Ginzburg-Landau formula.

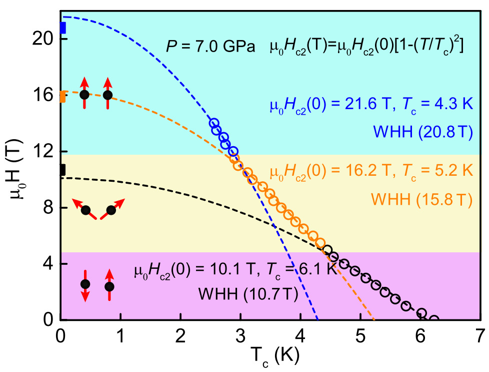

Fig. 5 Ginzburg-Landau (GL) fittings of the upper critical field μ_0H_{c2}s at 7.0 GPa. The circles are superconducting transition temperatures T_cs of $EuTe_2$ determined from resistance at 7.0 GPa. The pink, yellow, and blue regions correspond to the antiferromagnetic order, spin flop, and spin flipped states. The black, orange, and blue dashed lines represent corresponding GL fittings. The T_cs, fitted μ_0H_{c2}s using the GL formula, and the Werthamer-Helfand-Hohenberg formula for each magnetic state has been labeled.

$22\,\mathrm{T} - \mu_0H_J = \mu_0H_P$. The μ_0H_J and μ_0H_P with values of 13 and 9 T could be derived, respectively. If we assume the H_J is comparable with that of $EuTe_2$, the μ_0H_{c2} for the spin flipped state in the LP phase of $EuTe_2$ should be $10.1 + 13 \approx 23$ T, close to the fitted μ_0H_{c2} of 21.6 T from the GL formula. Through DFT calculations, the localized Eu 4*f* electrons reside ~1.25 eV below the Fermi level for the LP phase, while the Te 5*p* electrons crossing the Fermi level involve SC cooper pairing (Supplementary Note 10), consistent with the Jaccarino-Peter mechanism.

In summary, we have studied the structural and electronic transport properties of $EuTe_2$ under pressure. $EuTe_2$ shows a SC transition above 5 GPa with a maximum T_c of 6.1 K at 7.0 GPa and a structural transition at 16 GPa. The transition temperature of the *C*-type AFM order is enhanced in compressed $EuTe_2$ due to the increase of the magnetic exchange interactions. In the LP phase, superconductivity coexists with the AFM, spin flop, and spin flipped states. However, the electronic states of Eu^{2+} are well below the Fermi level and do not involve cooper pairing directly. The local moments of Eu^{2+} in the spin flop and spin flipped states produce an exchange field, compensating with the external field and resulting in an ultra-high upper critical field that is larger than the Pauli limit. The HP phase is nonmagnetic and the $\mu_0H_{c2} - T_c$ relation could be described by the GL formula with the μ_0H_{c2} within the Pauli limit. Our results establish that $EuTe_2$ is a pressure-induced superconductor with a high upper critical field which could be understood by the Jaccarino-Peter mechanism.

Methods

Single-crystal growth and neutron diffraction. Bulk single crystals of $EuTe_2$ were grown by the self-flux method. Pure Eu and Te were combined in the molar ratio of 1:10 and sealed in an evacuated quartz ampoule. The ampoule was slowly heated to 850 °C in 100 h and held for 75 h, then slowly cooled to 450 °C in 300 h. The shiny black single crystals of $EuTe_2$ were separated from the Te flux at 450 °C. The structure of $EuTe_2$ was confirmed by single-crystal XRD.

The powder neutron diffraction experiments were carried out on the Xingzhi triple-axis spectrometer at the China Advanced Research Reactor[40]. Powder samples were stuck on an aluminum foil uniformly with a hydrogen-free glue to reduce the absorption of Eu, then sealed in a cylindrical vanadium container and loaded into a closed cycle refrigerator that regulates the sample temperature from 3.5 to 300 K. A neutron velocity selector was used upstream to cleanly remove higher order neutrons for the incident neutron energy fixed at 16 meV.

High-pressure XRD. The in situ high-pressure synchrotron powder XRD patterns of $EuTe_2$ were collected at 300 K with an x-ray wavelength of 0.6199 Å on the Beijing Synchrotron Radiation Facility, Institute of High Energy Physics, Chinese Academy of Sciences. A symmetric diamond anvil cell with a pair of 300 μm diameter culets was used. A sample chamber with a diameter of 120 μm was drilled by laser in a pre-indented steel gasket. The $EuTe_2$ single crystals were ground into fine powders and compressed into a pellet with an 80 μm diameter and 20 μm thickness. The pellet was loaded into the middle of the sample chamber and silicone oil was used as a pressure-transmitting medium. A ruby sphere was also loaded into the sample chamber and pressure was determined by measuring the shift of its fluorescence wavelength. The data were initially processed using *Dioptas*[41] (with a CeO_2 calibration) and the subsequent Rietveld refinements were managed using *TOPAS*-Academic[42].

High-pressure magnetic and electrical property measurements. Magnetic and electrical measurements were taken on a physical property measurement system (PPMS, Quantum Design). High-pressure electrical transport measurements of $EuTe_2$ single crystals were carried out using a miniature diamond anvil cell made from a Be–Cu alloy on a PPMS. Diamond anvils with a 400 μm culet were used, and the corresponding sample chamber (with a diameter of 150 μm) was made in an insulating gasket achieved by cubic boron nitride and epoxy mixture. NaCl powders were employed as the pressure-transmitting medium, providing a quasi-hydrostatic environment. The pressure was also calibrated by measuring the shift of the fluorescence wavelength of the ruby sphere, which was loaded in the sample chamber. The standard four-probe technique was adopted for these measurements.

Theoretical calculations. Our structure searching simulations are performed by the swarm-intelligence-based *CALYPSO* (Crystal structure AnaLYsis by Particle Swarm Optimization) method, which enables global minimization of energy surfaces by merging ab initio total-energy calculations[22]. The structure searching was carried out at pressures of 5, 15, and 25 GPa which covers the experimental pressure range. The simulation cell sizes of 1−4 formula units were set. The underlying ab initio structural relaxations were carried out using density functional theory within the Perdew–Burke–Ernzerhof exchange-correlation[43] as implemented in the Vienna ab initio Simulation Package (*VASP*) code[44,45].

DFT calculations are performed using the *VASP* at the level of the generalized gradient approximation[43,46]. We adopted the projector augmented wave pseudopotentials and a plane-wave cutoff energy of 500 eV[44]. The experimentally measured lattice constants are used in our calculations and the positions of all atoms are fully relaxed until the force on each atom is less than 0.01 $eVÅ^{-1}$. We use $U = 4.4$ eV for Eu^{2+} ions because of the strong correlation among f electrons. The T_N of the pressurized $EuTe_2$ is obtained through parallel tempering Monte Carlo (MC) simulations[47,48].

Data availability

The source data and related supporting information are available upon reasonable request from the corresponding author.

Received: 5 September 2022; Accepted: 21 February 2023;
Published online: 01 March 2023

References

1. Bardeen, J., Cooper, L. & Schrieffer, J. Microscopic theory of superconductivity. *Phys. Rev.* **106**, 162–164 (1957).
2. Si, Q., Yu, R. & Abrahams, E. High-temperature superconductivity in iron pnictides and chalcogenides. *Nat. Rev. Mater.* **1**, 16017 (2016).
3. Scalapino, D. J. A common thread: The pairing interaction for unconventional superconductors. *Rev. Mod. Phys.* **84**, 1383 (2012).
4. Fernandes, R. M. et al. Iron pnictides and chalcogenides: a new paradigm for superconductivity. *Nature* **601**, 35–44 (2022).
5. Stewart, G. R. Unconventional superconductivity. *Adv. Phys.* **66**, 75–196 (2017).
6. Dai, P. Antiferromagnetic order and spin dynamics in iron-based superconductors. *Rev. Mod. Phys.* **87**, 855–896 (2015).
7. Ran, S. et al. Extreme magnetic field-boosted superconductivity. *Nat. Phys.* **15**, 1250–1255 (2019).
8. Ran, S. et al. Nearly ferromagnetic spin-triplet superconductivity. *Science (80-.)* **365**, 684–687 (2019).
9. Gammel, P. C. C. L., Bishop, D. J., Canfield, P. C., Gammel, P. L. & Bishop, D. J. New magnetic superconductors: a toy box for solid-state physicists. *Phys. Today* **51**, 40–46 (1998).
10. Yu, J., Le, C., Li, Z. & Li, L. Coexistence of ferromagnetism, antiferromagnetism, and superconductivity in magnetically anisotropic $(Eu,La)FeAs_2$. *npj Quantum Mater.* **6**, 63 (2021).
11. Jin, W. T. et al. Phase diagram of Eu magnetic ordering in Sn-flux-grown $Eu(Fe_{1-x}Co_x)_2As_2$ single crystals. *Phys. Rev. B* **94**, 184513 (2016).
12. Yin, J. et al. Large negative magnetoresistance in the antiferromagnetic rare-earth dichalcogenide $EuTe_2$. *Phys. Rev. Mater.* **4**, 13405 (2020).
13. Yang, H. et al. Colossal angular magnetoresistance in the antiferromagnetic semiconductor $EuTe_2$. *Phys. Rev. B* **104**, 214419 (2021).
14. Pan, X. C. et al. Pressure-driven dome-shaped superconductivity and electronic structural evolution in tungsten ditelluride. *Nat. Commun.* **6**, 7805 (2015).
15. Cai, W. et al. Pressure-induced superconductivity and structural transition in ferromagnetic $CrSiTe_3$. *Phys. Rev. B* **102**, 144525 (2020).
16. Yu, F. H. et al. Elevating the magnetic exchange coupling in the compressed antiferromagnetic axion insulator candidate EuIn2As2. *Phys. Rev. B* **102**, 180404 (2020).
17. Sun, H. et al. Magnetism variation of the compressed antiferromagnetic topological insulator $EuSn_2As_2$. *Sci. China Phys. Mech. Astron.* **64**, 118211 (2021).
18. Yang, P. T. et al. Pressured-induced superconducting phase with large upper critical field and concomitant enhancement of antiferromagnetic transition in $EuTe_2$. *Nat. Commun.* **13**, 2975 (2022).
19. Jaccarino, V. & Peter, M. Ultra-high-field superconductivity. *Phys. Rev. Lett.* **9**, 290 (1962).
20. Wang, Y. et al. An effective structure prediction method for layered materials based on 2D particle swarm optimization algorithm. *J. Chem. Phys.* **137**, 224108 (2012).
21. Wang, Y., Lv, J., Zhu, L. & Ma, Y. Crystal structure prediction via particle-swarm optimization. *Phys. Rev. B—Condens. Matter Mater. Phys.* **82**, 1–8 (2010).
22. Wang, Y., Lv, J., Zhu, L. & Ma, Y. CALYPSO: A method for crystal structure prediction. *Comput. Phys. Commun.* **183**, 2063–2070 (2012).
23. Coelho, A. A. TOPAS and TOPAS-Academic: an optimization program integrating computer algebra and crystallographic objects written in C++. *J. Appl. Crystallogr.* **51**, 210 (2018).
24. Ohara, H. et al. Charge ordering in Eu_3S_4 determined by the valence-difference contrast of synchrotron X-ray diffraction. *Phys. B Condens. Matter* **350**, 353–365 (2004).
25. Sugimoto, T. et al. Bcc-fcc structure transition of Te. *J. Phys. Conf. Ser.* **500**, 192018 (2014).
26. Jamieson, J. C. & Mcwhan, D. B. Crystal structure of tellurium at high pressures. *Phys. Today* **43**, 1149 (2014).
27. Clogston, A. M. et al. Upper limit for the critical field in hard superconductors. *Phys. Rev. Lett.* **9**, 266–267 (1962).
28. Akiba, K. et al. Magnetotransport properties of tellurium under extreme conditions. *Phys. Rev. B* **101**, 245111 (2020).
29. Akahama, Y. et al. Pressure-Induced sperconductivity and phase transition. *Solid State Communications* **84**, 803–806 (1992).
30. Qi, Y. et al. Pressure-driven superconductivity in the transition-metal pentatelluride HfTe5. *Phys. Rev. B* **94**, 054517 (2016).
31. Zhang, J. L. et al. Pressure-induced superconductivity in topological parent compound Bi_2Te_3. *Proc. Natl. Acad. Sci. USA* **108**, 24–28 (2011).
32. Malliakas, C. D., Chung, D. Y., Claus, H. & Kanatzidis, M. G. Superconductivity in the narrow-gap semiconductor $CsBi_4Te_6$. *J. Am. Chem. Soc.* **135**, 14540 (2013).
33. Butch, N. P. et al. Expansion of the high field-boosted superconductivity in UTe_2 under pressure. *npj Quantum Mater.* **6**, 75 (2021).
34. Jiao, L. et al. Chiral superconductivity in heavy-fermion metal UTe_2. *Nature* **579**, 523 (2020).
35. Duan, C. et al. Resonance from antiferromagnetic spin fluctuations for superconductivity in UTe_2. *Nature* **600**, 636 (2021).
36. Li, Z. et al. Superconductivity above 200 K discovered in superhydrides of calcium. *Nat. Commun.* **13**, 2863 (2022).
37. Werthamer, N. R., Helfand, E. & Hohenberg, P. C. Temperature and purity dependence of the superconducting critical field, Hc2. III. Electron spin and spin-orbit effects. *Phys. Rev.* **147**, 295–302 (1966).
38. Brian Maple, M. Induction of superconductivity by applied magnetic fields. *Nature* **315**, 95 (1985).
39. Meul, H. W. et al. Observation of magnetic-field-induced superconductivity. *Phys. Rev. Lett.* **53**, 497 (1984).
40. Cheng, P. et al. Nuclear instruments and methods in physics research a design of the cold neutron triple-axis spectrometer at the China Advanced Research Reactor. *Nucl. Inst. Methods Phys. Res. A* **821**, 17–22 (2016).
41. Prescher, C. & Prakapenka, V. B. DIOPTAS: a program for reduction of two-dimensional X-ray diffraction data and data exploration. *High. Press. Res.* **35**, 223–230 (2015).

42. Coelho, A. A. Computer programs TOPAS and TOPAS-Academic: an optimization program integrating computer algebra and crystallographic objects written in C ++. *J. Appl. Crystallogr.* **51**, 210 (2018).
43. Perdew, J. P., Burke, K. & Ernzerhof, M. Generalized gradient approximation made simple. *Phys. Rev. Lett.* **77**, 3865–3868 (1996).
44. Joubert, D. From ultrasoft pseudopotentials to the projector augmented-wave method. *Phys. Rev. B* **59**, 1758 (1999).
45. Kresse, G. & Furthmüller, J. Efficiency of ab-initio total energy calculations for metals and semiconductors using a plane-wave basis set. *Comput. Mater. Sci.* **6**, 15–50 (1996).
46. Vargas-Hernández, R. A. Bayesian optimization for calibrating and selecting hybrid-density functional models. *J. Phys. Chem. A* **124**, 4053–4061 (2020).
47. Lou, F. et al. PASP: Property analysis and simulation package for materials. *J. Chem. Phys.* **154**, 114103 (2021).
48. Hukushima, K. & Nemoto, K. Exchange Monte Carlo method and application to spin glass simulations. *J. Phys. Soc. Jpn.* **65**, 1604–1608 (1996).

Acknowledgements

This work at Sun Yat-Sen University was supported by the Guangdong Basic and Applied Basic Research Funds (Grant No. 2021B1515120015), National Natural Science Foundation of China (Grants No. 12174454, No. 12104518, No. 22090041, No. 92165204, No. 12074426, and No. 11227906), Guangzhou Basic and Applied Basic Research Funds (Grant No. 202201011123), Guangdong Provincial Key Laboratory of Magnetoelectric Physics and Devices (Grant No. 2022B1212010008), National Key Research and Development Program of China (Grant No. 2019YFA0705702), the Fundamental Research Funds for the Central Universities, Sun Yat-sen University (Grant No. 22QNTD3004) and the Research Funds of Renmin University of China (Grant No. 22XNKJ40). The work at Rice University is supported by the US Department of Energy, Basic Energy Sciences, under grant no. DE-SC0012311 and by the Robert A. Welch Foundation grant no. C-1839 (P.D.). We appreciate the support of BSRF, IHEP, CAS for high-pressure XRD measurements.

Author contributions

M.W. and H.S. proposed and designed the research. H.S. carried out the high-pressure measurements and data analysis with the help of Y.H, C.H, N.L, M.H., L.L., H.L., Z.L., and M.L. Single crystals were synthesized by C.H. Theoretical calculations were carried out by L.Q., Y.Z., W.W., D.Y., and Y.H. Neutron diffraction measurements were conducted by P.C. with the support of H.Z., H.W., and L.H. M.W., H.S., and P.D. wrote the paper with input from all co-authors. M.W. oversaw the project.

Competing interests

The authors declare no competing interests.

Additional information

Supplementary information The online version contains supplementary material available at https://doi.org/10.1038/s42005-023-01155-7.

Correspondence and requests for materials should be addressed to Meng Wang.

Peer review information *Communications Physics* thanks the anonymous reviewers for their contribution to the peer review of this work. Peer reviewer reports are available.